Prospects for magnetic field communications and location using quantum sensors

V. Gerginov,[1, 2, a)] F. C. S. da Silva,[2] and D. Howe[2]

[1)] *Department of Physics, University of Colorado, Boulder, CO 80309, USA*

[2)] *Time and Frequency Division, National Institute of Standards and Technology, 325 Broadway, Boulder, CO 80305, USA*

(Dated: 13 February 2018)

Signal attenuation limits the operating range in wireless communications and location. To solve the reduced range problem, we can use low-frequency signals in combination with magnetic sensing. We propose the use of an optically-pumped magnetometer as a sensor, and realize a proof-of-principle detection of binary phase shift keying (BPSK) modulated signals. We demonstrate a ranging enhancement by exploiting both the magnetometer's intrinsic sensitivity of below $1\,\mathrm{pT/Hz^{1/2}}$ and its 1 kHz operating bandwidth through the use of BPSK signals.

PACS numbers: 84.40.Ua, 07.07.Df, 32.80.Xx, 07.55.Ge

Keywords: communications, location, remote sensing, optically-pumped magnetometer

[a)] Electronic mail: Vladislav.Gerginov@nist.gov.

I. INTRODUCTION

Communications and location technologies are based primarily on the generation, transmission and reception of electromagnetic signals. In certain cases, the environment can distort, attenuate or even completely prevent the signals from propagating between transmitter and sensor. Specifically, AC electromagnetic fields have a high attenuation in metals, solid materials (concrete, rock, soil, etc.) and water. The electromagnetic field propagating through a given material is attenuated exponentially with the skin depth δ, given by the expression $\delta = (1/\pi f \mu_r \mu_\circ \sigma)^{1/2}$, where f is the field frequency, $\mu_\circ = 4\pi \times 10^{-7}$ is the magnetic constant, μ_r is the relative magnetic permeability of the material, and σ is the material conductivity[1]. According to this expression, the skin depth in the same material is three orders of magnitude smaller for $f = 1\,\mathrm{GHz}$ signal versus $f = 1\,\mathrm{kHz}$. This shows the advantage of using low-frequency signals in the presence of strong medium absorption. For example, signal attenuation inside buildings, underground or in water makes the conventional methods of communication and location, based on high-frequency transmission and reception, impractical or impossible.

We propose the use of low-frequency magnetic signals for communications and location in the presence of strong signal attenuation. The use of low frequencies comes at the price of reduced bandwidth (BW), leading to limited communication channel capacity and location accuracy. Another drawback is the long wavelength of the signal, and the large characteristic size of the antennae used for the most efficient RF link between transmitters and sensors, even when induction coils with ferrite cores are used to boost the signal above the thermal background. An example of using low-frequency electromagnetic fields is the Ultra Low Frequency (ULF) submarine communications system, the only successfully deployed underwater electromagnetic application[2]. Finally, the low-frequency magnetic fields have a dipole nature, and the field strength drops with the third power of the distance r (with r large compared to the dipole source size), thus reducing the signal range. For certain applications, the short signal range is useful as it allows multiple transmitters to be operated in close proximity without creating significant interference problems, and is the reason why local magnetic signal communications have recently attracted attention, for example for near-field magnetic field communication[3] and RFID tagging[4].

Magnetic field detection covers an enormous spectrum of applications - scientific, medical,

military, and space[5]. The range of magnetic field strengths in different applications spans 15 orders of magnitude - from Tesla fields used in nuclear magnetic resonance (NMR) and magnetic resonance imaging (MRI) experiments, to femtotesla (10^{-15}) fields generated by the brain activity. Most often the applications are limited to the detection of naturally occurring magnetic signals, and the use of magnetic signals to transfer information has been limited, mostly due to the short signal range of magnetic signals, the low frequency, and the presence of ambient noise. Examples of the use of magnetic signals for communication are through-the Earth[6], near-field magnetic induction[3], underwater[7] and even through the human body[8] communications. The navigation examples concern Global Positioning System (GPS)-denied environments and are based on either passive methods using "world maps" (Earth's field)[9], or active ones using artificially-created fields[10].

We propose a way to extend the range of low-frequency magnetic field signals by significantly increasing the sensitivity of the magnetic field sensors and by efficiently using their bandwidth. The highest magnetic field sensitivity has been demonstrated by Superconducting Quantum Interference Devices (SQUIDs)[11], and optically-pumped magnetometers (OPMs)[12], both reaching sensitivities below $1\,\mathrm{fT/Hz^{1/2}}$. The OPMs have the advantage of room-temperature operation, small size and low power and cost. It has been shown that they achieve orders of magnitude better sensitivities than induction coils with the same footprint[13], and can be operated in an unshielded environment at sensitivities significantly below the ambient magnetic field noise level[14]. Magnetometers configured to detect alternating magnetic fields in the MHz range[15] find use in applications such as NMR, MRI, magnetic induction imaging[13,16,17] and AC magnetic signature of machinery[18]. Chip-scale devices have been developed[19] and are being used in biomedical research[20–23] and low-field NMR[24]. Magnetometers with sensitivities below $10\,\mathrm{fT/Hz^{1/2}}$ and footprints of $14{\times}21{\times}80\,\mathrm{mm^3}$[23] and $19{\times}27{\times}60\,\mathrm{mm^3}$[25] recently became commercially available.

We present results of an OPM-based, single-channel, low data rate RF communications link and a link budget using a binary phase shift keying (BPSK) modulation scheme. The sensor demonstrates a sensitivity below $1\,\mathrm{pT/Hz^{1/2}}$ (significantly below the typical level of ambient magnetic field noise) in either a scalar or a vector sensor mode which requires no hardware modification. We demonstrate phase-sensitive detection of AC magnetic field signals with magnitude at the picotesla ($10^{-12}\,\mathrm{T}$) level and frequencies below 1 kHz. The BPSK modulation techniques fully utilize the sensor bandwidth of $\sim$1kHz to suppress the

ambient noise at 60 Hz and its harmonics, and to increase the channel capacity. Finally, we perform link calculation analysis to estimate communication and location ranging limits using low-frequency magnetic signal transmission.

II. COMMUNICATIONS AND LOCATION LINK.

We now derive the signal and noise link budgets needed to evaluate the performance of the system investigated here. Each budget has four parts: A) Signal Generation and Processing, B) Magnetic Flux Concentrators, C) Transmitter Antenna, D) OPM sensor. The resulting signal-to-noise (SNR) budget is included in the channel capacity formulation of the link and evaluated for purposes of communications and location.

A. Signal Generation and Processing

The signal generation, transmission and detection are always accompanied by noise. Here we list only the most relevant sources of noise encountered in magnetic signal generation and detection, in connection with the unique advantage of magnetic field data transmission - the full control of the spectral and temporal properties of the transmitter. The first type of noise results from the time varying fluctuations of the $\sim$50 μT geomagnetic field in the extremely low frequency (ELF, atmospheric science definition) band between 3 Hz and 3 kHz. This noise is on the order of 100 pT/Hz$^{1/2}$ at a given spatial point, and has a skin depth, or is correlated, over a range between 10 m to 1 km[26]. The noise in this band is mostly due to lightning activity in the neutral atmosphere, and is of random nature. The second type of noise is artificial (created by human activity, such as electrical power grid noise at 50/60 Hz and corresponding harmonics, transformers, machinery) and its spectrum can be deterministic. While the magnitude of the power grid harmonics can exceed the level of the geomagnetic noise and be above 1 nT, its sources are often local and are of dipole nature. A third type of noise is created by conductive objects, such as the Johnson noise[27], which has a broadband frequency spectrum. It can be significant at the position of the sensor and comparable in magnitude to the noise sources described above when it comes from objects in immediate sensor proximity.

To systematically reduce the influence of such environmental noise sources, we developed

a signal structure that naturally filters the grid noise and averages other uncorrelated time fluctuations by using a BPSK modulation scheme. Here the carrier signal has its phase switch between 0 and 180 degrees at the amplitude zero crossing by a pseudo-random sequence of m binary digits (chips) known as the "code" at chip rate ν_c. The value of m in decibels gives the processing gain. The code is designed to spread across the operational spectrum of the magnetometer and have notches of zero amplitude at all multiples of the grid fundamental frequency thus working as a digital filter of the grid harmonics. This filter function also averages uncorrelated time-domain noise via the two-point correlation function between the measured magnetometer signal and the pseudo-random code. This two-point correlation operation also produces a delta function in time that can be used to measure the time of arrival (or phase delay) between the source and the sensor. The amplitude of the delta function is proportional to m whereas all other correlation peaks scale with $\sqrt{m}$.

B. Magnetic Flux Concentrators

Concentrators are passive elements that rely on the constitutive relations between the magnetic field $\vec{H}$ and the magnetic induction $\vec{B}$ for their operation. In the absence of any medium $\vec{B} = \mu_\circ \vec{H}$. In the magnetostatic approximation (see Transmitter Antenna section), the presence of a medium contributes to the magnetic induction $\vec{B}$ through the magnetization $\vec{M}$

$$\vec{B} = \mu_\circ(\vec{H} + \vec{M}), \tag{1}$$

where $\vec{M} = \chi\vec{H}$ and χ is the magnetic susceptibility tensor. In general, χ is of rank 1 (scalar) and uniform in space. Nonetheless, the exact spatial relationship between $\vec{B}$ and $\vec{H}$ is complicated by the dipole nature of $\vec{M}$ combined with the boundaries of the concentrator medium and is quantified by the demagnetizing tensor D. Analytical expressions exist only for ellipsoids where D is diagonal and constant[28] and for rectangular shapes[29]. Numerically calculated tables for D are also available for cylinders[30].

The strength of the transmitted and received magnetic signals can be suitably amplified by means of flux concentrators with negligible noise penalties[31]. The concentrator gain G_c is thus a function of the relative magnetic permeability $\mu_r = (1+\chi)$ and the geometry of the material. In OPMs G_c can be as high as 20 with noise floors between $1 - 20\,\mathrm{fT}/\sqrt{\mathrm{Hz}}$ within the 20 Hz to 100 Hz bandwidth for ferrite-based concentrators[32]. Note that concentrators are

only effective if they can amplify signals to levels above the sensor equivalent input noise.

C. Transmitter Antenna

Because OPMs operate at frequencies below 1 kHz, electromagnetic fields at those frequencies have wavelengths greater than 300 km and thus for a range $r < 1$ km propagation effects are negligible. Therefore Maxwell's equations in free space approximate to $\nabla \times \vec{H} = \nabla \cdot \vec{H} = 0$. This is known as the magnetostatic approximation and allows a transmitter coil with p turns, area A and carrying a current I to behave like a magnetic dipole having a magnetic moment of

$$\vec{\mu} = \mu_{\circ} p I A \, \vec{n}, \tag{2}$$

where $\vec{n}$ is the vector normal to the coil area. This approximation holds if the coil size R is much smaller than the measurement range. The magnetic induction of a static dipole field is given by[1]

$$\vec{B} = \frac{3(\vec{\mu} \cdot \vec{r})\vec{r}}{r^5} - \frac{\vec{\mu}}{r^3}, \tag{3}$$

where $\vec{r}$ is the vector connecting the coil center of mass to the magnetometer. The ratio of the magnetic induction amplitude at r normalized by its corresponding value at R is the gain due to the propagation medium

$$G_m = \frac{cos\theta}{(r/R)^3}, \tag{4}$$

where $cos\theta = \vec{\mu} \cdot \vec{r}/(\mu\, r)$ and $r/R \gg 1$.

D. OPM sensor

Our choice of a scalar optically-pumped magnetometer as a magnetic field sensor is motivated by several factors. Scalar magnetometers have typical sensitivities below 1 pT/Hz$^{1/2}$[33], which is better than their solid-state counterparts[34] and is significantly below the ambient magnetic field noise in an unshielded environment[26]. They do not require calibration, and could combine small size, weight and power at a low cost[19]. Most importantly, they can be all-optical, reducing possible effects from cross-talk and allowing arrays of magnetometers to be built. The scalar magnetometer sensor in this work uses optical resonance excitation

(so-called Bell-Bloom configuration[35]), and detection of light polarization rotation[36]. While we choose amplitude modulation and detection of light polarization rotation, the magnetometer can also work with frequency-modulated light and transmission detection as well (at the expense of loss of sensitivity), reducing the device's complexity and power consumption.

The magnetometer is shown schematically in Fig. 1. Its design and operation is similar to that of the pulsed scalar magnetometer described elsewhere[37]. The magnetometer uses a glass vapor cell from Triad Technology[38] with 33 mm^3 internal volume, filled with isotopically-pure ^{87}Rb and 66.7 kPa (500 Torr) nitrogen acting as a buffer gas. The cell is heated to 358 K (85 ^{o}C) to increase the Rb density. The cell is enclosed in a single-layer magnetic shield, allowing easier experimental control of the ambient magnetic field compared to the case of unshielded environment. The shielding factor is between 10 and 20, and increases with the magnetic field frequency. A static magnetic bias magnetic field B_0 is applied along the z-axis, perpendicular to the cell's axis aligned along the x-axis, with a pair of Zeeman coils positioned inside the magnetic shield. An external modulation field can be applied with a speaker coil (not shown in Fig. 1) positioned outside the shield at a distance of 20 cm from the cell, with its axis aligned with the bias field direction.

Two 780 nm laser beams propagate through the cell, almost parallel to each other. The pump laser beam propagates at a small angle with respect to the x-axis in the xy-plane. It is circularly polarized and can be amplitude-modulated depending on the mode of operation. The amplitude modulation is accomplished by sending a train of 80 MHz pulses from a function generator to an RF amplifier, followed by an acousto-optic modulator. The beam optical frequency is red-detuned by ∼1.2 GHz from that of the unperturbed ^{87}Rb $F = 2 \rightarrow F' = 1$ transition, and is in resonance with the pressure-broadened ^{87}Rb D_2 line in the vapor cell. The probe laser beam propagates along the x-axis. It is linearly polarized, and its frequency is red-detuned by 9 GHz from the unperturbed ^{87}Rb $F = 2 \rightarrow F' = 1$ transition. The polarization of the far detuned probe laser beam with ∼150μW power exiting the cell is detected with a balanced polarimeter[36].

The magnetometer can operate and is evaluated in three modes of operation: DC (DC), zero-field (ZF), and self-oscillating (SO) modes. The DC and ZF modes could be used to detect magnetic field modulation (magnetic field signals). The SO mode is more useful in monitoring changes in the total magnetic field. The freedom to switch back and forth from a total field to a field component OPM sensor without any hardware modification could be

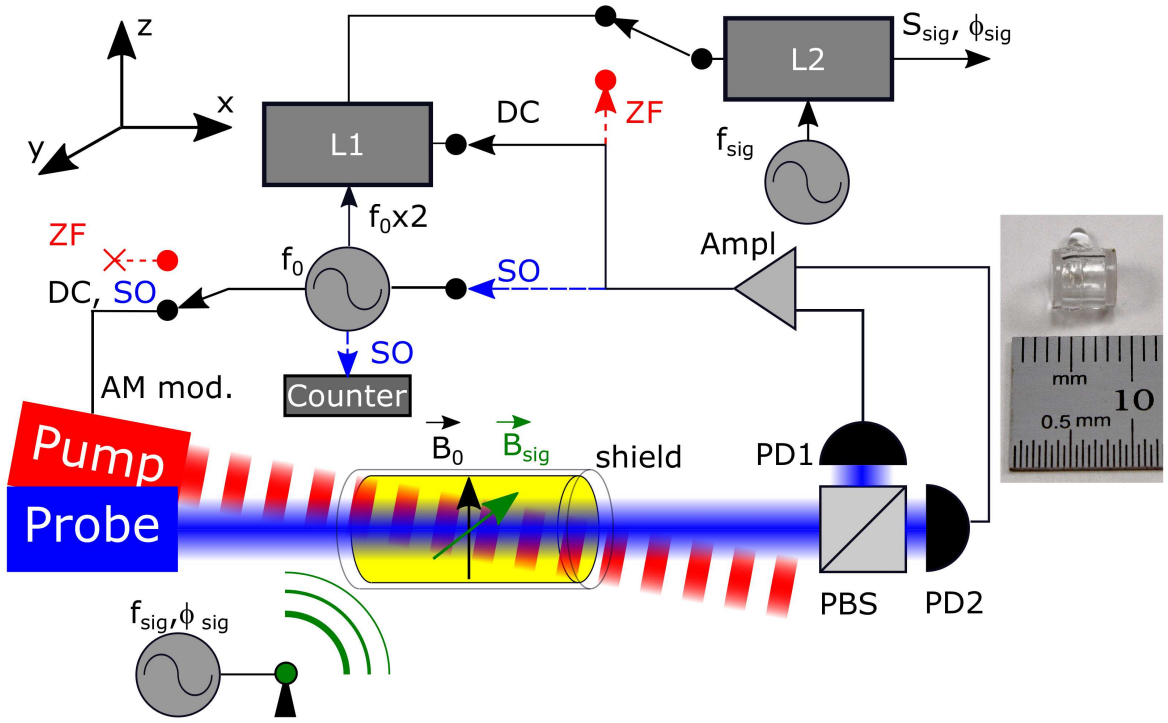

FIG. 1. Magnetic field sensor setup. The signal routes for the three magnetometer configurations are shown with solid (DC, black), dashed (SO, blue) and dotted (ZF, red) lines. PD - photodetector, PBS - polarizing beamspliter, L - lock-in amplifier, Ampl - amplifier. A picture of the vapor cell is shown on the right.

used to gain additional information about the vector properties of the magnetic signal and the ambient magnetic field noise. The modes of operation are summarized in Table I.

In the DC mode of operation (the nominal mode of operation used in this work), a static magnetic field $|B_0| = 14$ μT is applied, corresponding to Larmor precession frequency of 98 kHz. The pump laser beam is modulated at half the Larmor frequency[37]. The resonance between the light modulation and the Larmor precession[35] causes modulation of the probe light polarization. The polarization modulation signal is detected with a lock-in amplifier $L1$, referenced to the second harmonic of the modulation frequency. The quadrature signal from the lock-in amplifier becomes sensitive to the difference between the modulation frequency and half of the precession frequency, caused by changes in the total magnetic field magnitude

TABLE I. Modes of operation of the scalar magnetometer with relevant parameters. In the DC and SO modes, the magnetometer is most sensitive in the direction of the bias field $\vec{B}_0$. In the ZF mode, the magnetometer is most sensitive in the plane perpendicular to the x- (or light-) axis. [a)]The band means range of measured DC fields. [b)]The sensitivity is expressed as magnetic field instability $\sim 1/\sqrt{\tau}$, with τ the measurement time.

Mode	Band	Sensitivity pT/Hz$^{1/2}$	Measured property	Transduction type
DC	DC-1 kHz	0.2	$\left\vert\vec{B}_0 + \vec{B}_{\rm sig}\right\vert$	T $\rightarrow$ V (DC)
ZF	DC-1 kHz	0.2	$\left\vert\vec{B}_{\rm sig}\right\vert_\perp$	T $\rightarrow$ V (AC)
SO	10^{-9}-10^{-6} T [a)]	2.0 [b)]	$\left\vert\vec{B}_0 + \vec{B}_{\rm sig}\right\vert$	T $\rightarrow$ Hz

at the cell position. Thus the output of the lock-in amplifier $L1$ contains information about the signal magnetic field vector $\vec{B}_{\rm sig}$, which adds to the static magnetic field vector $\vec{B}_0$. The use of a second lock-in amplifier $L2$, phase-synchronized with the frequency of the transmitter's signal, outputs a signal with magnitude $S_{\rm sig}$ and phase $\phi_{\rm sig}$, which are related to the transmitted field $\vec{B}_{\rm sig}$. The detected signal magnitude $S_{\rm sig}$ depends on the mutual orientation of $\vec{B}_0$ and $\vec{B}_{\rm sig}$, and the distance and attenuation between the transmitter and sensor.

In the ZF mode of operation, the magnitude of the static magnetic field at the magnetometer's position is set to zero. The pump laser beam is not modulated, and it creates atomic polarization along its direction (x-axis). The probe polarization has a maximum rotation. The presence of magnetic field $\vec{B}_{\rm sig}$ at the cell position causes the atomic polarization to precess away from the direction of the pump beam, which decreases the degree of atomic polarization in this direction. The rotation of the probe light polarization also changes. Thus the polarimeter detects a zero-field resonance[39], and its output can be demodulated directly by lock-in amplifier $L2$ to obtain $S_{\rm sig}$ and $\phi_{\rm sig}$. The detected signal magnitude $S_{\rm sig}$ depends on the orientation and the magnitude of $\vec{B}_{\rm sig}$, and its orientation with respect to the pump/probe axis, and will be in general different from the signal magnitude detected in the DC mode due to the absence of a bias field $\vec{B}_0$. The ZF field mode offers reduced experimental complexity, eliminating the need for the high dynamic range lock-in amplifier $L1$ and its reference. On the other hand, the total field magnitude in unshielded operation

must be maintained below the magnetometer's resonance linewidth (<200 nT), which might require periodic implementation of a total field zeroing procedure[40,41]. This mode can also be used to detect magnetic field modulation signals.

The magnetic field noise in DC and ZF modes measured by the magnetometer is shown in Fig. 2. In the DC mode, the values of modulation frequency on resonance and the gyromagnetic ratio were used to calibrate the magnetic field magnitude $|B_0|$, and to convert the lock-in amplifier $L1$ output voltage noise to magnetic field noise. The calibration was done by introducing a small deviation of the modulation frequency away from resonance (which is equivalent to a change of the bias field away from the resonance), and observing the voltage change at the lock-in amplifier output. When the bias field magnitude $|B_0|$ is significantly different from the resonance, the measured noise provides information about the magnetometer noise floor. The on-resonance curve (Fig. 2, (A)) shows the ambient-dominated magnetic field noise at 2 pT/Hz$^{1/2}$ level. The magnetic noise due to the power lines causes the resonances at 60 Hz and its harmonics.

In the ZF mode, the bias magnetic field and the pump beam modulation are turned off. The power in the pump and probe beams was optimized to increase the magnetometer sensitivity. An external AC magnetic test field at 210 Hz frequency was applied along the direction of the bias field using the speaker coil. The calibration field is orthogonal to the x-axis, and has the same amplitude in both DC and ZF modes. The 210 Hz calibration signal is only visible in the on-resonance case (Fig. 2, (A) and (C)). The calibration field was used to determine the sensitivity of the magnetometer in ZF mode, in the absence of spin precession. The voltage noise at the polarimeter output was converted to magnetic field noise using the known calibration field magnitude. The on-resonance curve (Fig. 2, (C)) shows agreement with the corresponding DC mode curve (Fig. 2, (A)) except for the roll-off at higher frequencies, due to the time constant of 100 μs of the lock-in amplifier $L1$ (used only in the DC mode).

To study the limit of the magnetometer sensitivity, the bias magnetic field was detuned far from resonance, while the modulation frequency was kept the same. The off-resonant curves (Fig. 2, (B) and (D)) show a magnetometer noise floor and sensitivity limit significantly below 1 pT/Hz$^{1/2}$ for both configurations. The expected magnetometer sensitivities are significantly below the ambient magnetic field noise level of 2 pT/Hz$^{1/2}$, indicating that magnetic data transmission is not limited by the magnetometer even in the presence of

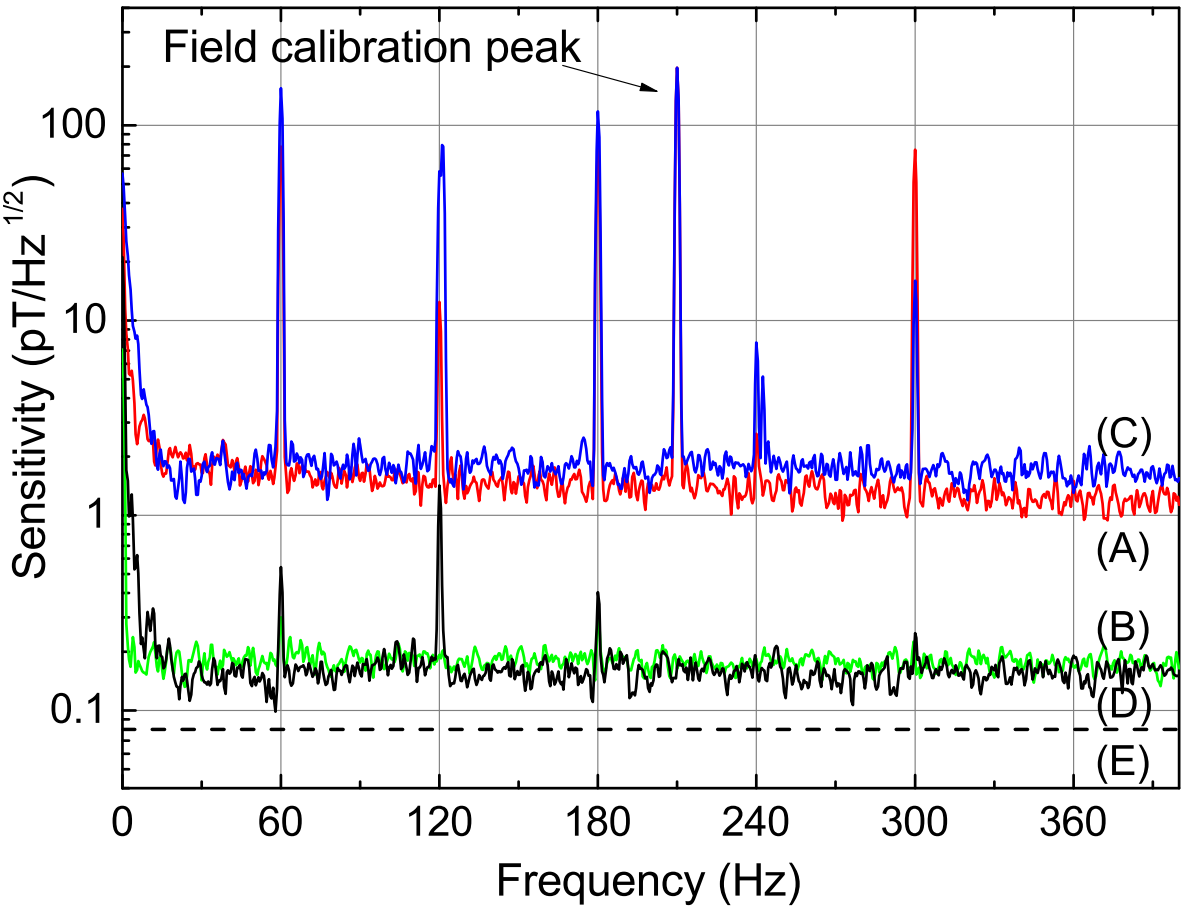

FIG. 2. Magnetometer sensitivity as a function of frequency. DC mode: (A) - on resonance, (B) - off-resonance. ZF mode: (C) - on resonance, (D) - off-resonance. The dashed line (E) shows the measured level of electronics noise in the absence of light. The calculated probe light photon shot noise is at the same level.

a magnetic shield. The dashed line (E) represents the measured electronics noise in the absence of light. The calculated photon shot noise due to the probe beam is at the same level. Previous results[37] indicate that the magnetometer sensitivity should reach 200 fT/Hz$^{1/2}$ in a cell of this volume. A sensitivity of 100 fT/Hz$^{1/2}$ in an unshielded environment has already been demonstrated[14], and this limit has been used in the channel capacity calculations below as an OPM baseline.

In the SO mode of operation, the reference for the amplitude modulation is phase-locked to the rectified polarimeter output. Changes of the magnetic field magnitude $|B_0|$ lead to a change of the precession frequency, and thus to a change of the pump beam modulation

frequency. The modulation frequency becomes phase-locked to the precession frequency and thus to the magnetic field magnitude $|B_0|$. A frequency counter is used to calibrate the absolute value of $|B_0|$ using the gyromagnetic ratio $\gamma = 2\pi \times 7$ Hz/nT for ^{87}Rb. The output of the polarimeter is rectified using a fast comparator, and is used to trigger the amplitude modulation of the pump laser beam after an appropriate phase delay. The function generator is set up to provide only one pump pulse during two Larmor precession periods, which fulfills the condition for pumping at a subharmonic of the precession frequency. The polarimeter signal, containing a frequency component corresponding to the Larmor precession period, was counted with a frequency counter with a gate time of 50 ms.

Figure 3 shows the results of magnetic field instability measurements performed in SO mode, expressed as an Allan deviation[42]. A measurement of the ambient field at the magnetometer position (Fig. 3, filled circles) shows field instability below 8 pT/$\tau^{1/2}$ (Fig. 3, long-dash curve). This is expected, considering that the SO magnetometer is sensitive to the integrated ambient magnetic field noise spectrum shown in (Fig. 2, (A) and (C)), which is above 2 pT/Hz$^{1/2}$ and contains 60 Hz harmonics above 100 pT/Hz$^{1/2}$. To approach the intrinsic magnetometer sensitivity, a phase-locked loop was used to lock the precession frequency to a frequency reference by controlling the magnitude of the bias magnetic field $|B_0|$. The precession frequency at the output of the polarimeter was compared with a stable 98 kHz signal referencing the lock-in amplifier $L1$. The $L1$ output was used to control the current through the bias field coils and the value of $|B_0|$, locking the Larmor precession frequency to 98 kHz. The phase-locked loop suppressed the magnetic field noise in the 100 Hz bandwidth, reducing the magnetic field measurement instability to 2 pT/Hz$^{1/2}$ (Fig. 3, short-dash curve), which is consistent with the ambient magnetic field noise floor away from the 60 Hz harmonics.

E. Single Channel Capacity

The signal S and noise N at the sensor, measured here in units of Tesla, can now be estimated based on the gain factors at the antenna and OPM via flux concentrators and through the propagating media. In conjunction with the signal processing gain represented by the used bandwidth BW, we can determine the communication or location ability of the

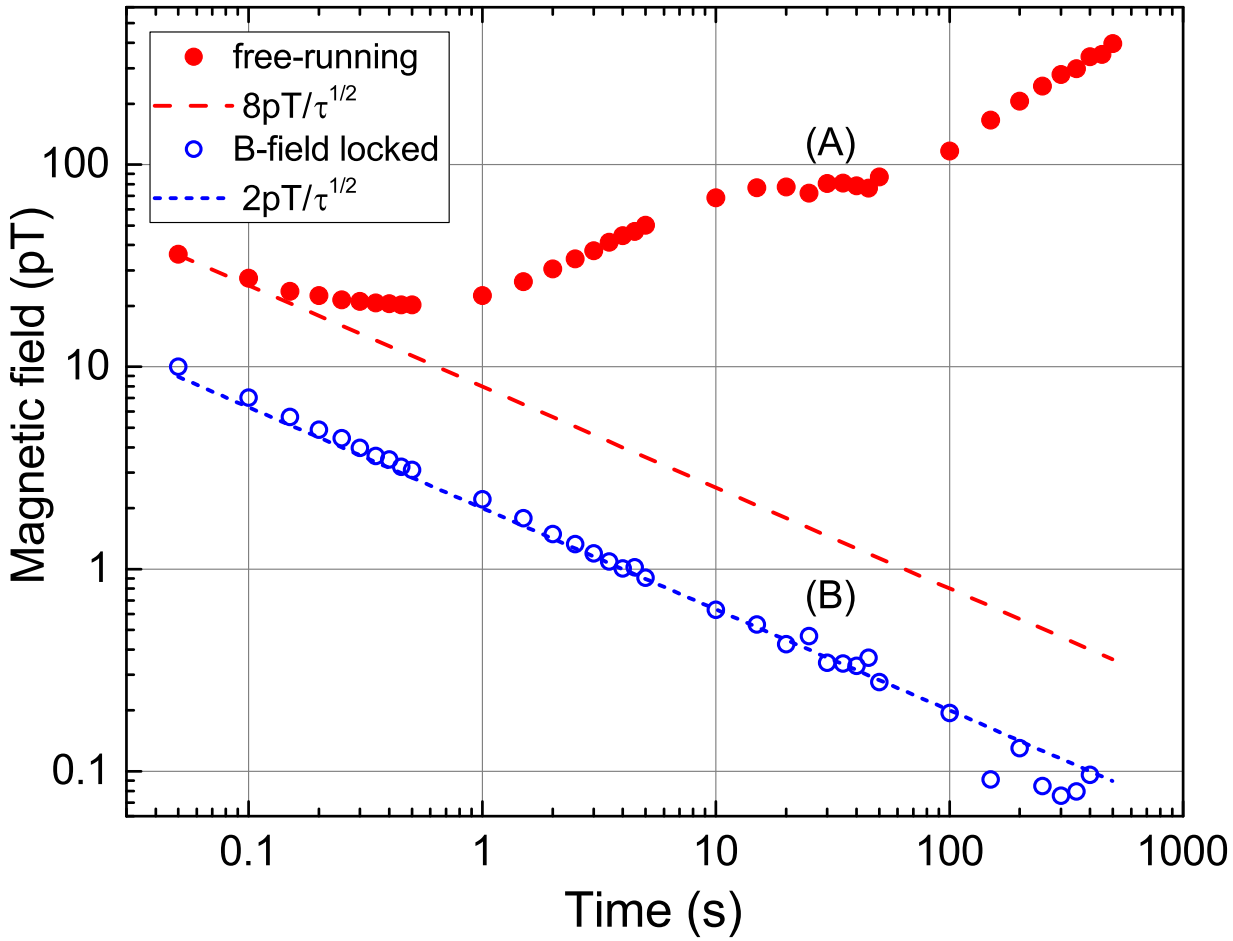

FIG. 3. Measured magnetic field instability in SO mode as a function of measurement time. Free-running magnetic field - (A), filled symbols. Projected white noise instability - 8 pT/$\tau^{1/2}$ - dashed (red) line. Phase-locked magnetic field - (B), open symbols. Projected white noise instability - 2 pT/$\tau^{1/2}$ - dotted (blue) line.

link via the channel capacity[43]

$$C = BW \log_2 \left(1 + (S/N)^2\right), \tag{5}$$

where the signal amplitude is $S = G_c^{Tx} \times G_m \times G_c^{Rx} \times Tx + Rx$ and the noise amplitude is $N = G_c^{Tx} \times G_m \times G_c^{Rx} \times N_{Tx} + N_{Rx}$, both at 1 Hz bandwidth. Here Rx is the baseline of the OPM and N_{Rx} is the ambient noise at the sensor. The S/N in Eq. 5 is squared to conform with the units of power normally used to calculate channel capacity. Typical numbers are: $Tx = 1\,\mathrm{mT}$, $Rx = 100\,\mathrm{fT}$, $N_{Tx} = 100\,\mathrm{nT}$, $N_{Rx} = 100\,\mathrm{pT}$, $G_c = 10$ using[32], $R = 0.1\,\mathrm{m}$, $\theta = 0$ assuming the transmitter and sensor can be aligned independently using

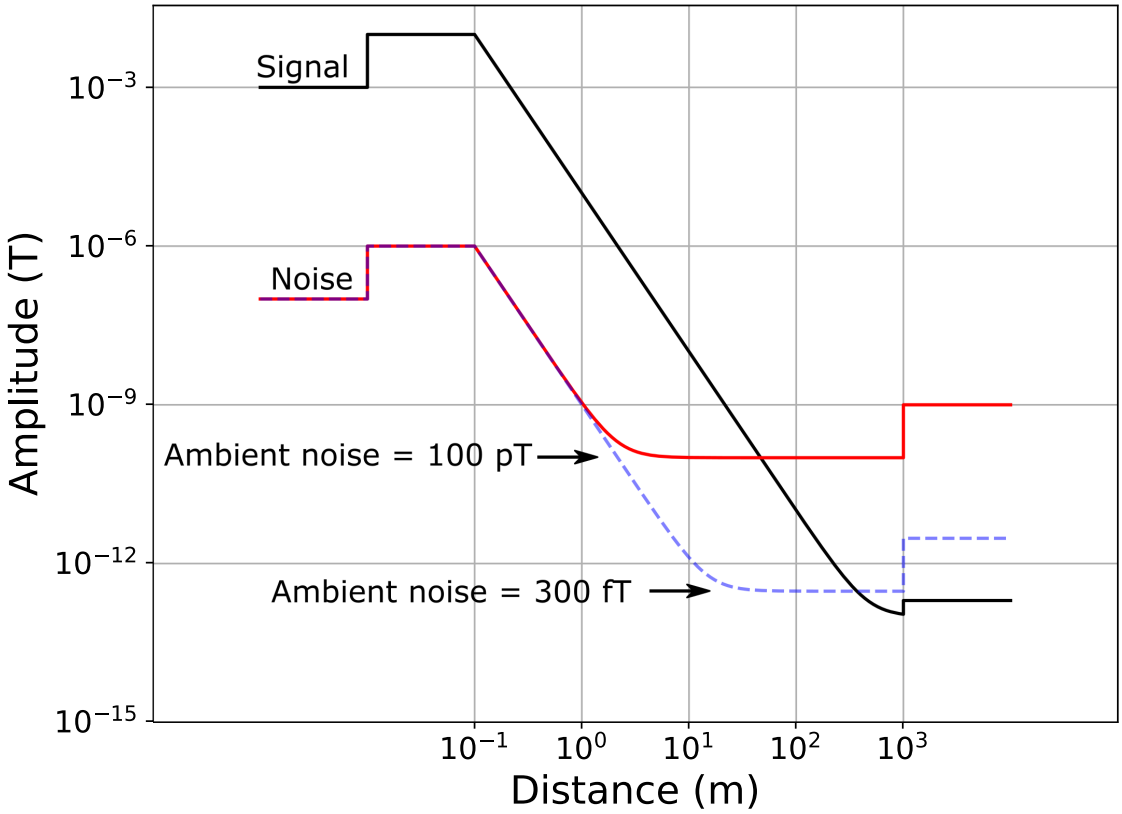

FIG. 4. Link calculation analysis for the magnetic field signal and noise (solid curves) at 1 Hz bandwidth. The ambient field noise of $N_{Rx} = 100\,\mathrm{pT}$ is determined by the Earth's magnetic field noise. The dashed curve represents a hypothetical situation of ambient noise reduced to $N_{Rx} = 300\,\mathrm{fT}$. The intersection of the signal and noise curves results in an SNR = 1. The steps in the curves are due to the concentrator gains.

the Earth's magnetic field direction as a reference. Figure 4 shows a graphical representation of Eq. 5 for the above parameters. The dashed curve represents a hypothetical situation where the ambient noise is at $N_{Rx} = 300\,\mathrm{fT}$, which could possibly be achieved by using a combination of OPM sensors with $N_{Rx} = 100\,\mathrm{fT}$ baseline as discussed in Section IV. The spatial range corresponding to SNR = 1 is tens of meters in the ambient noise-limited case ($N_{Rx} = 300\,\mathrm{fT}$), but could be extended to hundreds of meters if the noise is close to the sensor baseline. To calculate the maximum channel capacity at the sensor, we consider $BW = 1\,\mathrm{kHz}$ (OPM bandwidth).

TABLE II. Parameters of the detected magnetic modulation signals shown in Fig. 5. Column 2 - signal magnitude; column 3 - SNR; columns 4-6 - measured instability at $\tau = 1\,\mathrm{s}$, [a] using BPSK with a chip rate $\nu_c = 30\,\mathrm{Hz}$, [b] using BPSK with $\nu_c = 150\,\mathrm{Hz}$. The instability can be regarded as phase uncertainty and is reduced as $\nu_c^{1/2}$ increases, as shown in Columns 5 and 6.

Case	Magn.	SNR	Instab.	Instab.[a]	Instab.[b]
	pT		mrad/$\sqrt{\tau}$	mrad/$\sqrt{\tau}$	mrad/$\sqrt{\tau}$
A	35	25	30	5	2
B	20	14	40	7	3
C	10	7	80	15	7
D	3	2	1080	197	88

III. RESULTS

The proof-of principle evaluation of the scalar magnetometer-based OPM sensor was performed in the DC mode of operation, with a bias field of $14\,\mu$T. A single-tone magnetic signal at 150 Hz was created with the speaker coil. The signal varied in magnitude (cases (A) to (D)). The magnetic field spectrum (the output signal of $L1$ converted to magnetic field magnitude) is shown in Fig. 5, with the lock-in amplifier $L1$ time constant of $100\,\mu$s. The measured modulation magnitudes and signal-to-noise ratios (SNR) are given in the second and third column of Table II.

A phase-sensitive detection at the 150 Hz modulation frequency was performed with the lock-in amplifier $L2$ with a time constant of 300 ms. The phase instability of the transmitted signal reference and the $L2$ reference was much below the measured phase instability of the detected 150 tone, which was determined by the limited SNR. The measured phase instability at 1 s is given in the fourth column of Table II.

The 150 Hz signal phase at each signal magnitude was monitored over $\sim$50 000 s. The phase instability over the measurement time, expressed as Allan deviation[42], is shown in Fig. 6 with solid symbols. Due to the time constant of $L2$, the instability decreases below 1 s. The solid lines represent white noise-dominated measurements, scaling as $1/\tau^{1/2}$. They were calculated using the measured instability values at 4 s (Fig. 6, open symbols). The instabilities at 4 s are a compromise between values at short times, affected by the $L2$ time

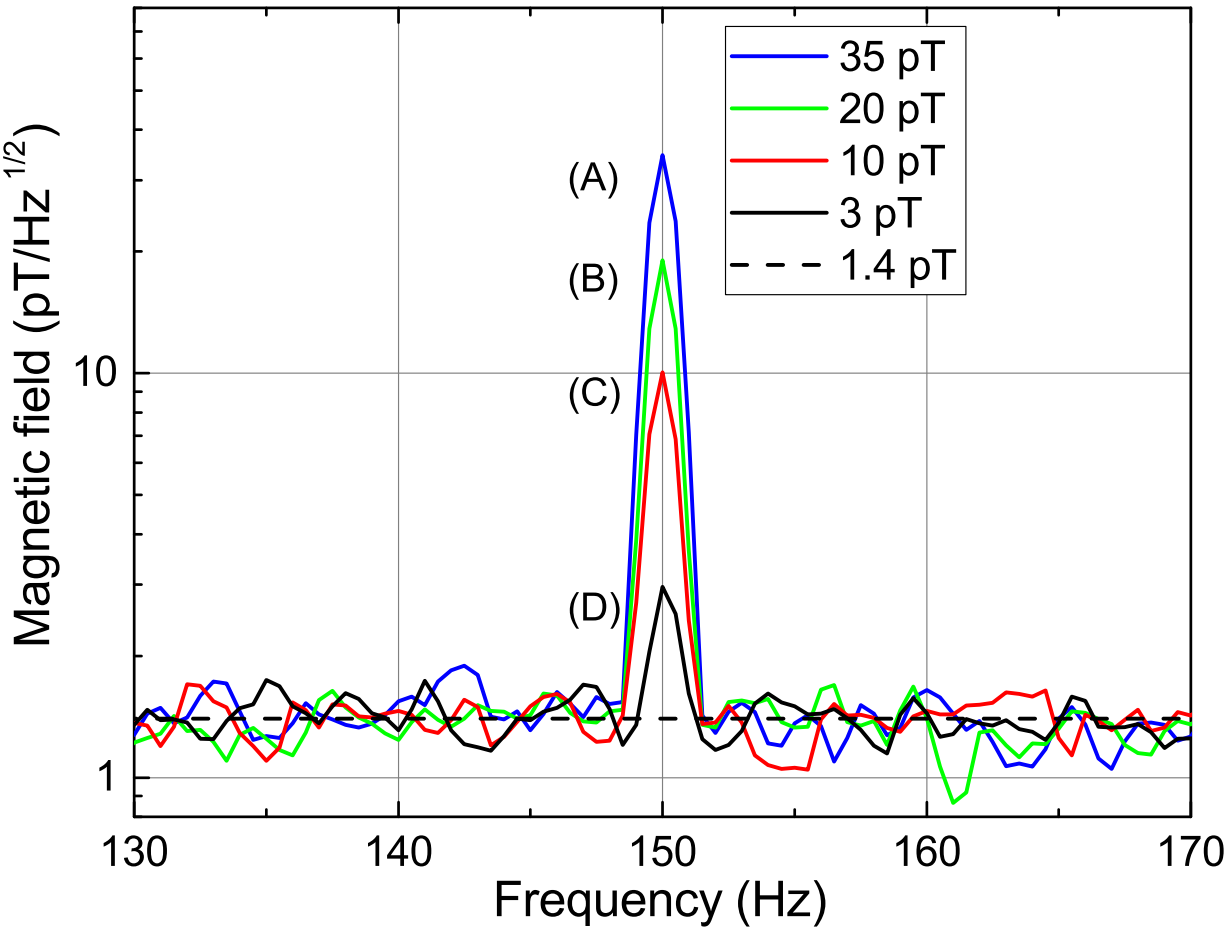

FIG. 5. OPM sensor output spectrum in the presence of a magnetic signal with 150 Hz frequency. (A) - 35 pT, (B) - 20 pT, (C) - 10 pT, (D) - 3 pT. The dashed line represents the ambient magnetic field noise of 1.4 pT. The magnetic signal magnitudes are given in Table II.

constant, and the long-term drifts apparent at times longer than 10 s. The corresponding instabilities at 1 s are given in the fourth column of Table II. The averaging period necessary to reach a given measurement accuracy can be calculated from the instabilities at 1 s. For the presented measurements, no attempt has been made to control experimental parameters such as laser frequencies, powers, or ambient magnetic field, and the deviation from the expected $1/\tau^{1/2}$ dependence is due in part to drifts in the parameters of the free-running OPM. It is worth mentioning that in certain cases, the phase instability follows $1/\tau^{1/2}$ dependence up to 10 000 s, reaching reliably the 1 mrad level even without active parameter control.

To utilize the sensor bandwidth, detection of phase-modulated signals was also performed

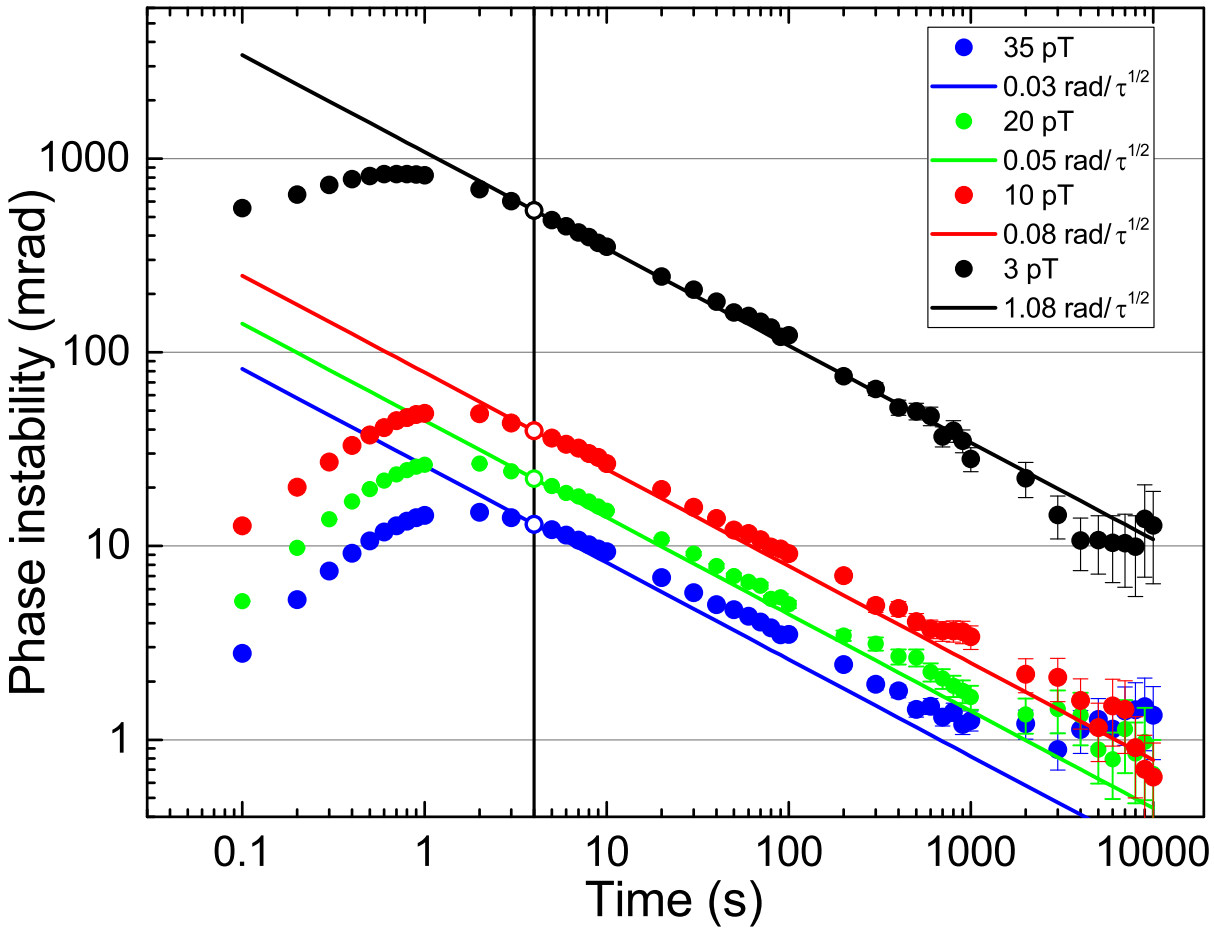

FIG. 6. Measured phase instability of the detected signals shown in Fig. 5 versus measurement time. Solid symbols - data, open symbols - 4 s data points used to calculate the projected $1/\tau^{1/2}$ white noise dependence (given with solid lines).

by BPSK modulation scheme, as discussed in Section II, A). First, a carrier frequency $\nu_\circ = 210$ Hz (case (A)) modulated with a chip rate $\nu_c = 30$ Hz. This was done intentionally to avoid 60 Hz power grid frequency and its harmonics. Second, a carrier frequency $\nu_\circ = 180$ Hz was modulated with a maximum chip rate of $\nu_c = 180$ Hz to maximize the use of the sensor bandwidth (case (B)). Both codes lasted 20 s, which creates notches at multiples of 0.05 Hz, thus also suppressing the power grid harmonics. Figure 7 shows the two BPSK modulation signal spectra used to excite the transmitter. Figure 7 also shows how the BPSK modulation uses the available spectrum of the sensor.

The spectrum of the detected BPSK modulated magnetic field signals is shown in Fig. 8. The shield attenuation, which increases with frequency, and the OPM sensor bandwidth,

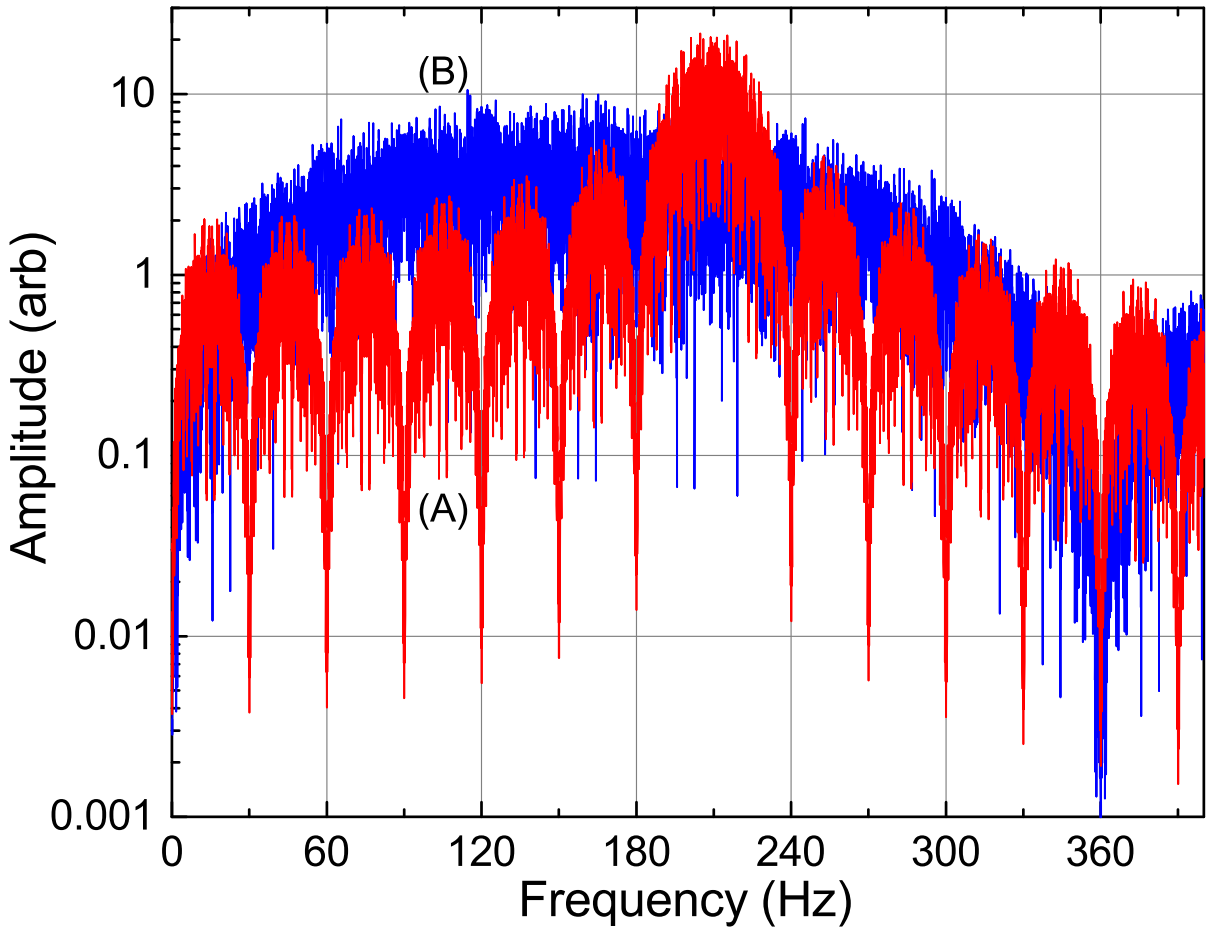

FIG. 7. BPSK modulation signal spectra. (A): $\nu_\circ = 210\,\text{Hz}$, $\nu_c = 30\,\text{chips/s}$, $m = 60$. (B): $\nu_\circ = 180\,\text{Hz}$, $\nu_c = 180\,\text{chips/s}$, $m = 3600$.

limit the spectrum amplitudes at frequencies above 300 Hz.

The signals were demodulated using $L2$, referenced to $\nu_\circ$. The phase detection signal is shown in Fig. 9. In the case (A), the beat signal between the closest 60 Hz harmonics and the $L2$ reference is visible as oscillations between consecutive phase flips. In the case (B), as $L2$ is referenced to a 60 Hz harmonic, no beat is apparent in the spectrum. The phase flips in the case (B) happen more often than in case (A) due to the higher chip rate ν_c, as indicated by the different horizontal span.

The response of the sensor to the BPSK-modulated signal was correlated with the original code. The correlation results as a function of the time delay between signal and code are shown in Fig. 10. The measured ratios between the correlation peak and the standard deviation of the background noise, and the square root of the number of chips m, are 26

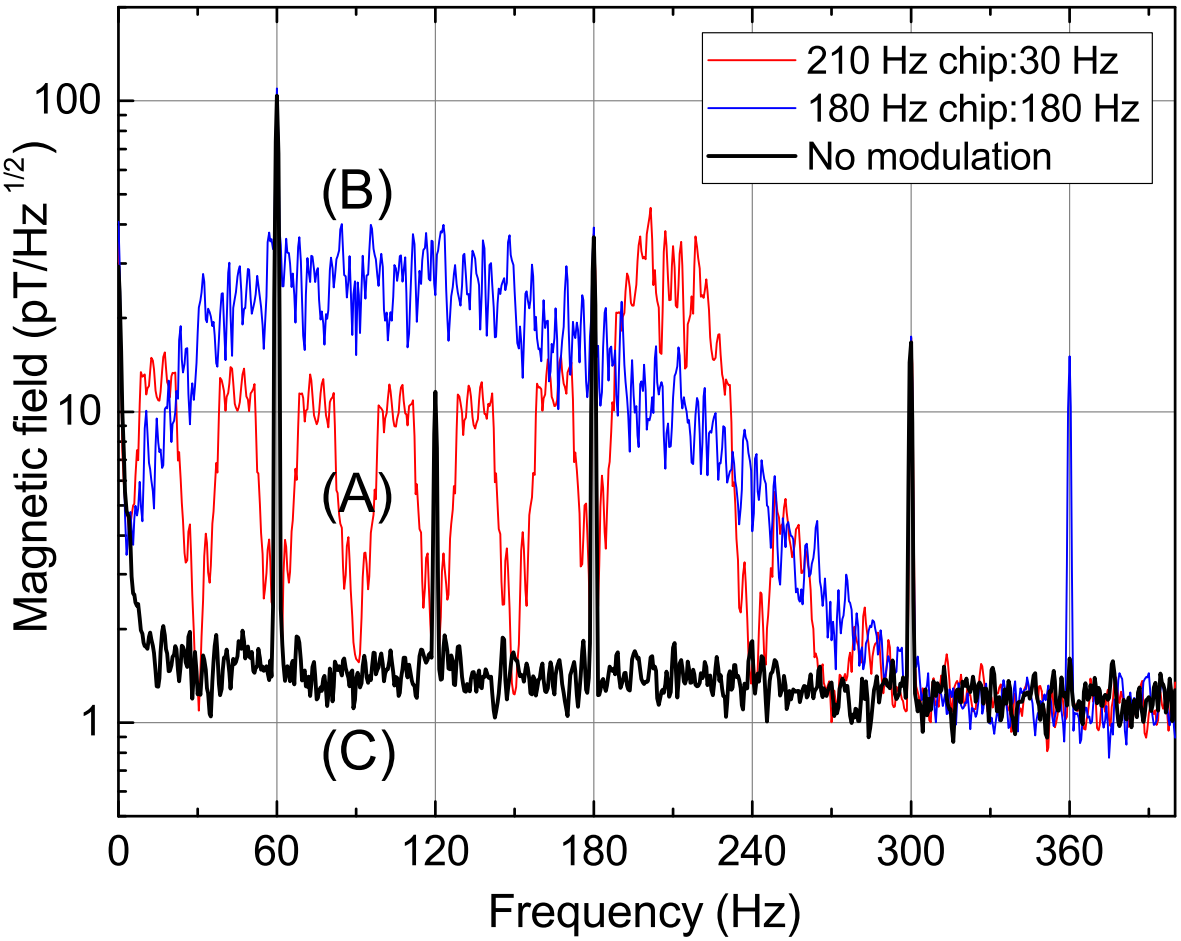

FIG. 8. sensor output spectrum in the presence of BPSK signals. (A): $\nu_\circ = 210\,\text{Hz}$, $\nu_c = 30\,\text{Hz}$. (B): $\nu_\circ = 180\,\text{Hz}$, $\nu_c = 180\,\text{Hz}$. (C) - no modulation. The spectra (A) and (B) correspond to the spectra shown in Figure 7. The signal magnitudes at higher frequencies are reduced as a result of the limited sensor bandwidth.

and 24 for the case (A), and 50 and 60 for the case (B), showing only a slight degradation of the measured SNR for the case (B).

The BPSK-modulated signal in the case (A) has both $\nu_\circ$ and ν_c correspond to the power line harmonics. At the output of lock-in amplifier $L2$, the closest power line harmonics cause demodulated signals at frequencies of 60 Hz or higher, which are rejected by the integration time of $L2$ of 300 ms. In the case (B), the BPSK-modulated signal has limited support at the power line harmonics. This can clearly be seen in Figures 7 and 8 (curves (B)). Since the signal correlation is done by the multiplication of the code and detected signal spectra, this limited support leads to a natural suppression of the power line harmonics in the correlated

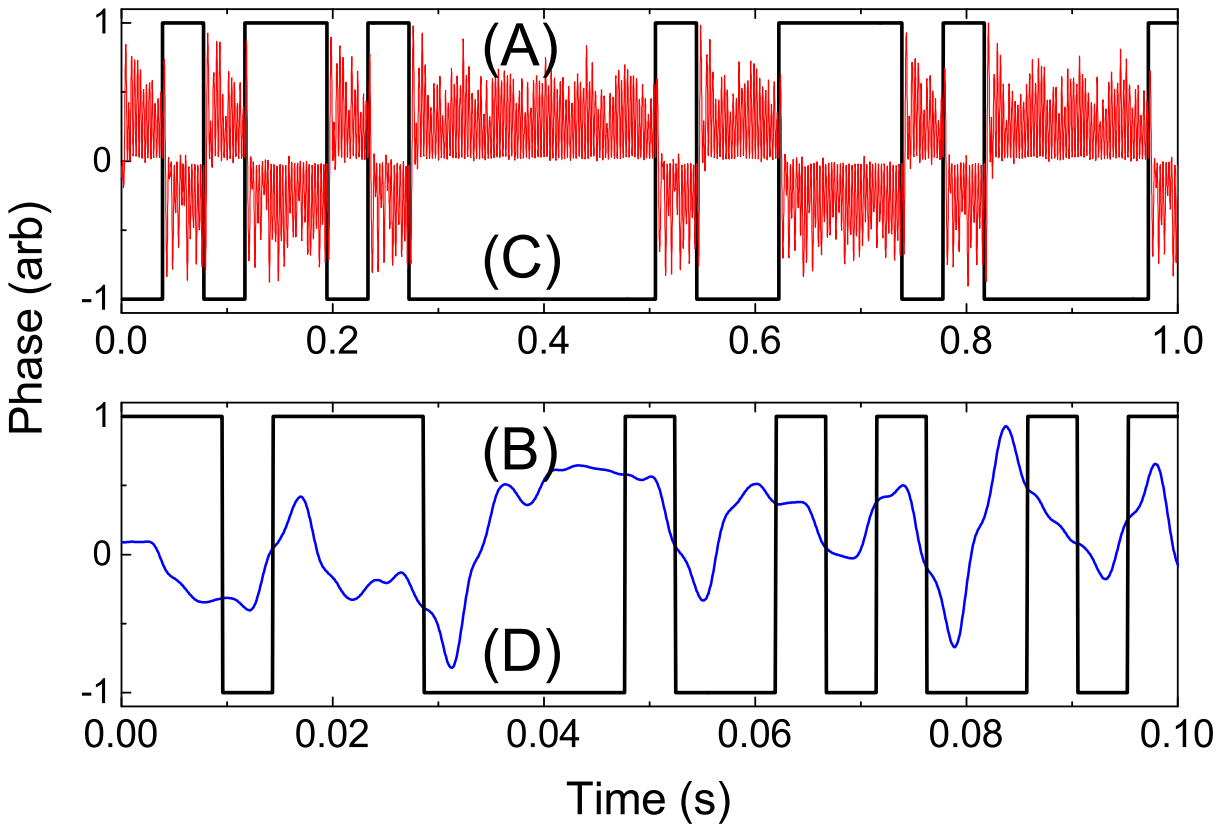

FIG. 9. Time dependence of the detected magnetic signal phase. (A): $\nu_\circ = 210\,\mathrm{Hz}$, $\nu_c = 30\,\mathrm{Hz}$. (B): $\nu_\circ = 180\,\mathrm{Hz}$, $\nu_c = 180\,\mathrm{Hz}$. (C): $\nu_c = 30\,\mathrm{Hz}$ code. (D): $\nu_c = 180\,\mathrm{Hz}$ code.

signal. Both modulation schemes offer the usage of significant part of the OPM sensor bandwidth, with detected signals largely unaffected by the power line harmonics.

The processing gain over a single-tone signal when BPSK-modulated signal is used, is given by $10\log_{10}\sqrt{\nu_c}$ at 1 s. Processing gain reduces the uncertainty of a phase or time delay determination to a fractional chip duration. The projected instabilities using BPSK modulation are given in Columns 5 (chip rate of 30 Hz) and 6 (chip rate of 180 Hz) of Table II, based on the measured single-tone instabilities at 1 s given in Column 4 of the same Table.

IV. DISCUSSION

The graphical representation of the link calculations shown in Figure 4 indicates the main contributions in the performance of the OPM - based signal transmission. We can now evaluate our results by considering two main applications for OPMs: communications and

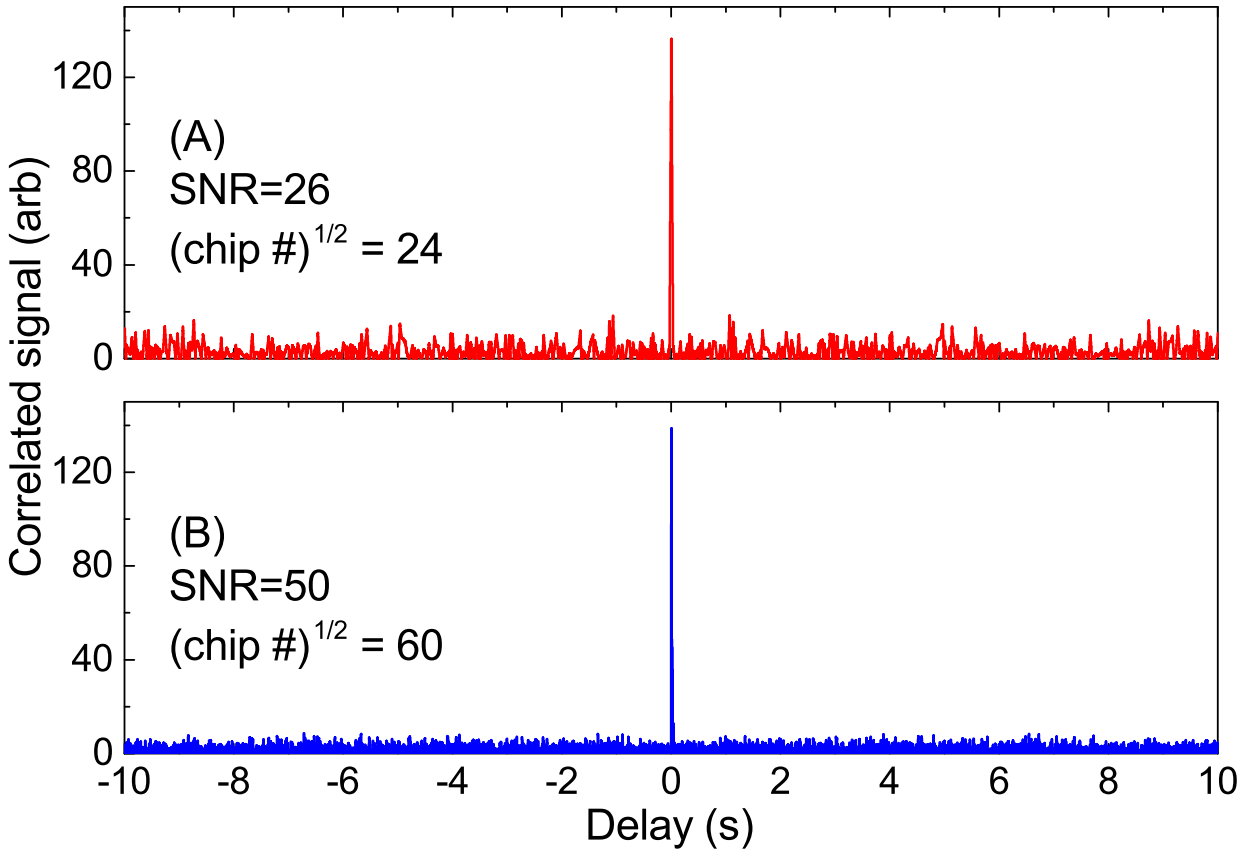

FIG. 10. Correlation between the demodulated signal and the BPSK code as a function of the time delay between the signal and the code. (A): $\nu_\circ = 210\,\mathrm{Hz}$, $\nu_c = 30\,\mathrm{Hz}$. (B): $\nu_\circ = 180\,\mathrm{Hz}$, $\nu_c = 180\,\mathrm{Hz}$.

location.

For communications, the channel capacity is the best performance metric since it directly measures the bit rate for a given range. We use the link budget described in Section II E and shown in Figure 4. With ambient noise-determined sensor baseline of $100\,\mathrm{pT}/\sqrt{\mathrm{Hz}}$ and SNR = 2 at the sensor (corresponding to the last row of Table II), the channel capacity is about 2.3 bits/s, achieved at a range of 37 m at 1 Hz bandwidth. For chip rates (or bandwidth) of 30 Hz and 180 Hz, the channel capacity is correspondingly 70 bits/s and 418 bits/s. With a sensor baseline of $300\,\mathrm{fT}/\sqrt{\mathrm{Hz}}$ (budgeting for ambient noise cancellation using more than one OPM with a $100\,\mathrm{fT}/\sqrt{\mathrm{Hz}}$ baseline), as shown in Fig. 4, these channel capacities would be obtained at 320 m range.

For location, the phase noise of the received signal is the relevant parameter since it

is related to the uncertainty in the measured phase delay. In vacuum, the phase delay uncertainty has to be less than 10 ns for a corresponding spatial uncertainty of less than 3 m. In media other than vacuum, this uncertainty decreases proportionally with the medium index of refraction. The phase noise measured with the OPM sensor and shown in Fig. 6 is dominated by the poor SNR, with the phase noise at 1 s tabulated in Table II. The phase noise of the transmitter and sensor frequency references can be neglected at the measured noise levels. Using the last row of Table II, single-tone frequency of 150 Hz and SNR = 2, the phase noise uncertainty of 1.08 rad (time delay uncertainty of 1.14 ms) at $\tau = 1$ s is reduced by averaging down to 10 mrad (11.4 μs) at integration time of 10 000 s (Fig. 6). At SNR = 25, the same phase delay uncertainty is reached in 10 s and is 1.1 μs at 1 000 s, after which the phase noise becomes independent of the averaging time due to drifts in the free-running OPM parameters.

To perform time averaging in real applications, digital signal generation and processing utilize the available bandwidth via BPSK modulation schemes. Using the BPSK processing gain (corresponding to an improvement factor of $\sqrt{\nu_c}$) with $\nu_c = 150$ Hz, for SNR = 2 the time delay uncertainty would be reduced to $\sim$100 μs in 1 s, and $\sim$1 μs at 10 000 s. Therefore, to obtain 10 ns of phase delay uncertainty in 1 s with a sensor baseline of 100 pT/$\sqrt{\text{Hz}}$ (the ambient noise), the range decreases to 2.3 m in vacuum. However with a sensor baseline of 300 fT/$\sqrt{\text{Hz}}$ (the OPM baseline), the range increases to 16 m.

It is important to stress that the signals measured by OPMs can penetrate media that displays orders of magnitude more loss at higher frequencies at the cost of lower bandwidth or more integration time. Therefore, comparisons with higher capacity channels or spatial location uncertainties should consider the propagation through such media as water, rock, snow and even metals.

Improvements in the link budget are possible by the reduction of the ambient noise and the OPM baseline, use of stronger field sources, and increasing the OPM operational bandwidth.

It is beyond the scope of this work to list all possible techniques for magnetic field signal generation, noise rejection, or sensor sensitivity/bandwidth improvement, and we only briefly mention some of them. Permanent $Nd_2Fe_{14}B$ neodymium magnets can produce dc magnetic inductions of the order of 1 T and can be mounted on actuators such as audio speakers or rotating platforms to produce signals with 1 kHz bandwidth. The use of concentrators

at the transmitter end is beneficial provided that the concentrator does not degrade the transmitter signal-to-noise ratio. However, the use of concentrators on the sensor end can enhance performance only if the OPM baseline is below the concentrated received signal and above the concentrated ambient noise, otherwise the ambient noise will be enhanced more than the received signal. Arguably, the most consequential contribution to the received signal reduction is the normalized range r/R where a change by a factor of two corresponds to a change by a factor of eight in signal strength.

Existing techniques for magnetic field noise rejection exploit the spatial, spectral and temporal properties of the noise sources. The most common noise cancellation technique is based on spatial noise rejection. The signal and noise could be spatially separated using sensor arrays to cancel the magnetic field noise from distant[44] and local[45] sources. For applications where the signal source is local, shielding and gradiometer techniques work best, and common-mode rejection ratios above 100 have been demonstrated[46]. For data transfer at a distance, this technique is not suitable, since gradiometers will have reduced sensitivity to a signal from a source at a distance large compared to the gradiometer baseline. Techniques for reducing the local noise when the signal source is remote are more appropriate, as it has been successfully demonstrated for example in space magnetometry[45]. Using arrays of sensors could allow spatial noise rejection, and could provide information about direction, distance, magnitude, and orientation of a local dipole source[47]. With respect to local noise sources such as power lines, transformers, machinery or thermal Johnson noise, care must be taken to position the sensor away from such sources. We can also explore the noise's spectral and temporal properties, and use signal frequencies where no significant noise components exist. The complete freedom to choose the properties of an artificially-created signal allows the application of multitude of techniques developed for phase detection, time and frequency dissemination, and communications. Signal properties in the time domain can be used to suppress uncorrelated noise[48]. Using digital signal processing techniques, we can filter out and/or average noise components in the spectral domain, as demonstrated in Section III.

The fundamental sensitivity of scalar optically-pumped magnetometers based on alkali atoms is estimated to be at $1\,\mathrm{fT}/(\mathrm{Hz}^{1/2}\,\mathrm{cm}^3)$[49] and even lower values have been demonstrated using pulsed regime of operation and quantum non-demolition detection with ^{87}Rb[33]. The measured sensitivity of our OPM corresponds to $40\,\mathrm{fT}/(\mathrm{Hz}^{1/2}\,\mathrm{cm}^3)$[37], and the calculated photon shot noise limit is $15\,\mathrm{fT}/(\mathrm{Hz}^{1/2}\,\mathrm{cm}^3)$, showing that further improvement of the OPM

sensor baseline is possible.

It is possible that even with noise suppression, the residual ambient noise will be higher than the OPM sensor baseline. In this case, the sensitivity of OPMs can be reduced to match the residual environmental noise levels by increasing the magnetometer bandwidth[50,51] and thus the channel capacity.

V. CONCLUSIONS

We investigate the use of low-frequency magnetic signals for communication and location applications. Compared to the case of traditionally used radio-frequency electromagnetic signals, their advantage in the presence of strong signal attenuation is in the extended spatial range. We use an optically pumped magnetometer operated as a sensor to achieve high detection sensitivity. The spatial range is mostly limited by the ambient noise, and could be extended to hundreds of meters if that noise is suppressed by the use of the available sensor sensitivity. We demonstrate a one-channel spread-spectrum signal processing technique to eliminate the systematic fluctuations coming from power grid harmonics and reduce the ambient noise by averaging uncorrelated fluctuations from the environment. We provide benchmarks and discuss methods of further improving the performance of this new technique.

ACKNOWLEDGMENTS

Sponsored by Public Safety Communications Research, Communications Technology Laboratory, NIST, Boulder, CO. U.S. Government document; not subject to copyright. We gratefully acknowledge support by Dereck Orr and Jeb Benson of the Public Safety Communications Research, Communications Technology Laboratory, NIST, Boulder, CO. We wish to thank Svenja Knappe, Sean Krzyzewski, Corey Barnes, Craig Nelson, and Archita Hati for the helpful discussions and the technical support.

REFERENCES

[1]J. D. Jackson, *Classical Electrodynamics*, 2nd ed. (John Wiley & Sons, 1975).

[2]L. L. Klessig and V. L. Strite, *The ELF odyssey : National Security Versus Environmental Protection* (Westview Press, 1980).

[3]W. Jiang, D. Ferreira, J. Ylioja, J. Goncalves, and V. Kostakos, in *Proceedings of the 2014 ACM International Joint Conference on Pervasive and Ubiquitous Computing*, UbiComp '14 (ACM, New York, NY, USA, 2014) pp. 261–265.

[4]Y. Chen, Z. Zheng, M. Gong, and F. Yu, *Sensors*, Sensors **17** (2017).

[5]P. Ripka, *Magnetic sensors and magnetometers* (Artech House Publishers, 2001).

[6]M. R. Yenchek, G. T. Homce, N. W. Damiano, and J. R. Srednicki, IEEE Transactions on Industry Applications **48**, 1700 (2012).

[7]I. F. Akyildiz, P. Wang, and Z. Sun, IEEE Communications Magazine **53**, 42 (2015).

[8]J. Park and P. P. Mercier, in *2015 37th Annual International Conference of the IEEE Engineering in Medicine and Biology Society (EMBC)* (2015) pp. 1841–1844.

[9]J. M. Wilson, R. J. Kline-Schoder, M. A. Kenton, P. H. Sorensen, and C. O. H., in *Proceedings of the 2006 National Technical Meeting of The Institute of Navigation January 18 - 20, 2006* (2006).

[10]J. Blankenbach and A. Norrdine, in *2010 International Conference on Indoor Positioning and Indoor Navigation* (2010) pp. 1–5.

[11]J. Clarke, International Journal of Modern Physics B: Condensed Matter Physics; Statistical Physics; Applied Physics **24**, 3999 (2010).

[12]D. Budker and M. Romalis, Nat Phys **3**, 227 (2007).

[13]I. Savukov, S. Seltzer, and M. Romalis, Journal of Magnetic Resonance **185**, 214 (2007).

[14]G. Bevilacqua, V. Biancalana, P. Chessa, and Y. Dancheva, Applied Physics B **122**, 1 (2016).

[15]I. M. Savukov, S. J. Seltzer, M. V. Romalis, and K. L. Sauer, Phys. Rev. Lett. **95**, 063004 (2005).

[16]I. M. Savukov and M. V. Romalis, Phys. Rev. Lett. **94**, 123001 (2005).

[17]C. Deans, L. Marmugi, S. Hussain, and F. Renzoni, Applied Physics Letters **108**, 103503 (2016).

[18]L. Marmugi, L. Gori, S. Hussain, C. Deans, and F. Renzoni, Appl. Opt. **56**, 743 (2017).

[19]P. D. D. Schwindt, S. Knappe, V. Shah, L. Hollberg, J. Kitching, L.-A. Liew, and J. Moreland, Applied Physics Letters **85**, 6409 (2004).

[20]H. Xia, A. Ben-Amar Baranga, D. Hoffman, and M. V. Romalis, Applied Physics Letters **89**, 211104 (2006).

[21]C. Johnson, P. D. D. Schwindt, and M. Weisend, Applied Physics Letters **97**, 243703 (2010).

[22]T. H. Sander, J. Preusser, R. Mhaskar, J. Kitching, L. Trahms, and S. Knappe, Biomedical Optics Express **3**, 981 (2012).

[23]E. Boto, S. S. Meyer, V. Shah, O. Alem, S. Knappe, P. Kruger, T. M. Fromhold, M. Lim, P. M. Glover, P. G. Morris, R. Bowtell, G. R. Barnes, and M. J. Brookes, NeuroImage **149**, 404 (2017).

[24]M. Ledbetter, C. Crawford, A. Pines, D. Wemmer, S. Knappe, J. Kitching, and D. Budker, Journal of Magnetic Resonance **199**, 25 (2009).

[25]R. J. Cooper, D. W. Prescott, P. Matz, K. L. Sauer, N. Dural, M. V. Romalis, E. L. Foley, T. W. Kornack, M. Monti, and J. Okamitsu, Phys. Rev. Applied **6**, 064014 (2016).

[26]C. Constable, Surveys in Geophysics **37**, 27 (2016).

[27]J. B. Johnson, Phys. Rev. **32**, 97 (1928).

[28]J. A. Osborn, Physical Review **67**, 351 (1945).

[29]A. Aharoni, Journal of Applied Physics **83**, 3432 (1998).

[30]D. X. Chen, J. A. Brug, and R. B. Goldfarb, IEEE Transactions on Magnetics **27**, 3601 (1991).

[31]A. Guedes, J. M. Almeida, S. Cardoso, R. Ferreira, and P. P. Freitas, IEEE Transactions on Magnetics **43**, 2376 (2007).

[32]W. C. Griffith, R. Jimenez-Martinez, V. Shah, S. Knappe, and J. Kitching, Applied Physics Letters **94**, 023502 (2009).

[33]D. Sheng, S. Li, N. Dural, and M. V. Romalis, Phys. Rev. Lett. **110**, 160802 (2013).

[34]P. Ripka and M. Janosek, IEEE Sensors Journal **10**, 1108 (2010).

[35]W. E. Bell and A. L. Bloom, Phys. Rev. Lett. **6**, 623 (1961).

[36]A. Gozzini, C. R. Hebd. Seances Acad. Sci. **255**, 1905 (1962).

[37]V. Gerginov, S. Krzyzewski, and S. Knappe, J. Opt. Soc. Am. B **34**, 1429 (2017).

[38]Any mention of commercial products is for information only; it does not imply recommendation or endorsement by NIST.

[39]J. Dupont-Roc, S. Haroche, and C. Cohen-Tannoudji, Physics Letters A **28**, 638 (1969).

[40]S. J. Seltzer and M. V. Romalis, Applied Physics Letters **85**, 4804 (2004).

[41]V. Shah and K. Hughes, "Method for detecting zero-field resonance," (2015), US Patent 9,116,201.

[42]D. W. Allan, IEEE Trans. Ultrason., Ferroelect., Freq. Control **34**, 647 (1987).

[43]C. E. Shannon, Proceedings of the IRE **37**, 10 (1949).

[44]H. Slack, M. Vance, and L. L. Lynch, Geophysics **32**, 877 (1967).

[45]N. F. Ness, K. W. Behannon, R. P. Lepping, and K. H. Schatten, Journal of Geophysical Research **76**, 3564 (1971).

[46]D. Sheng, A. R. Perry, S. P. Krzyzewski, S. Geller, J. Kitching, and S. Knappe, Applied Physics Letters **110**, 031106 (2017), http://dx.doi.org/10.1063/1.4974349.

[47]W. L. Goodman, V. W. Hesterman, L. H. Rorden, and W. S. Goree, Proceedings of the IEEE **61**, 20 (1973).

[48]W. E. Wickerham, Geophysics **19**, 116 (1954).

[49]S. Smullin, I. Savukov, G. Vasilakis, R. Ghosh, and M. Romalis, Phys. Rev. A **80**, 033420 (2009).

[50]V. Shah, G. Vasilakis, and M. V. Romalis, Phys. Rev. Lett. **104**, 013601 (2010).

[51]R. Jimenez-Martínez, W. C. Griffith, S. Knappe, J. Kitching, and M. Prouty, J. Opt. Soc. Am. B **29**, 3398 (2012).